

Parrondo paradox in quantum image encryption

Lukasz Pawela¹

¹*Institute of Theoretical and Applied Informatics,
Polish Academy of Sciences, Baltycka 5, 44-100 Gliwice, Poland**

We present a quantum image encryption protocol that harnesses discrete-time quantum walks (DTQWs) on cycles and explicitly examines the role of the Parrondo paradox in security. Using the NEQR representation, a DTQW-generated probability mask is transformed into a quantum key image and applied via CNOT to encrypt grayscale images. We adopt an efficient circuit realization of DTQWs based on QFT-diagonalization and coin-conditioned phase layers, yielding low depth for $N = 2^n$ positions and t steps. On 64×64 benchmark images, the scheme suppresses adjacent-pixel correlations to near zero after encryption, produces nearly uniform histograms, and achieves high ciphertext entropy close to the 8-bit ideal value. Differential analyses further indicate strong diffusion and confusion: NPCR exceeds 99% and UACI is around 30%, consistent with robust sensitivity to small plaintext changes. Crucially, we identify parameter regimes in which alternating coin operations induce the Parrondo paradox and degrade security by raising correlations, lowering entropy, and reducing NPCR/UACI, thereby constituting practical failure modes. Our results provide both a performant DTQW-based quantum image cipher and clear guidance on coin/message parameter selection to avoid paradox-dominated regimes. We discuss implications for hardware implementations and extensions to higher-dimensional walks.

I. INTRODUCTION

The secure transmission and storage of digital images is a fundamental requirement in modern information technology, especially in light of the emerging capabilities of quantum computing, which threaten to undermine classical cryptographic methods. Quantum image processing (QIP) leverages unique features of quantum mechanics such as superposition, entanglement, which emerge in high-dimensional Hilbert spaces to encode and protect visual information in ways unattainable by classical approaches [1].

Quantum image encryption schemes have advanced rapidly with the adoption of efficient quantum image representations such as the Novel Enhanced Quantum Representation (NEQR) [2], which allows for deterministic retrieval and flexible, pixel-level addressability of grayscale images [1]. A particularly promising approach involves the use of quantum walks, which are the quantum analogues of classical random walks and are characterized by quantum superposition, ballistic spreading, and the generation of entanglement. Discrete-time quantum walks (DTQWs) [3–5] (see [6] for a comprehensive review) are especially suitable for quantum circuit implementation due to their discrete nature, and have demonstrated utility in various quantum algorithms and cryptographic protocols [6–9].

In quantum image encryption, DTQWs can be exploited to generate complex, highly sensitive, and pseudo-random encryption keys. For example, the work [1] developed a protocol in which a quantum walk on a cycle is used to produce a quantum mask image, serving as the control in a quantum CNOT operation that

encrypts the NEQR image [1]. This methodology produces encryption schemes that are robust against standard cryptanalytic attacks and demonstrate strong statistical randomness and sensitivity to both key and plaintext.

The DTQW formalism involves a Hilbert space that is the tensor product of a position register and an internal coin register. Each time step consists of a quantum coin operation followed by a conditional shift, efficiently implemented in quantum circuits via the quantum Fourier transform (QFT) for diagonalizing the conditional shift operator [7]. Quantum walks are known for their periodic dynamics, recurrence, and the recurrent generation of entangled states, which are directly relevant for cryptographic applications [7, 10].

The Parrondo paradox [11–14], originally developed in game theory and statistical physics, describes the counterintuitive phenomenon where alternating between two losing strategies results in a winning outcome. Quantum analogues of Parrondo’s games, especially those involving quantum walks, display even richer behavior owing to quantum coherence and entanglement [15–17]. In particular, the paradox manifests in quantum walks on cycles and lines, where alternating quantum coin operations that individually produce a “losing” outcome can, when combined, yield a “winning” result [15, 16].

In this work, we present a quantum image encryption protocol that explicitly exploits the Parrondo paradox within the framework of quantum walks. We demonstrate how the alternation or controlled combination of individually suboptimal (or even insecure) quantum walk-based encryption strategies can paradoxically result in a robust, highly secure protocol. Central to our approach is the quantum walk representation: using efficient circuit implementations, we alternate different coin operations or parameters in the DTQW, producing an encryption mask whose security properties emerge from

* lpawela@iitis.pl

the paradoxical “winning” behavior observed in the combined quantum dynamics [16, 17]. We show how this method performs on a simulator, demonstrating its potential for real-world applications in quantum image encryption.

II. QUANTUM WALK IMPLEMENTATION

Quantum walks (QWs) are a quantum-mechanical generalization of classical random walks, playing a foundational role in quantum algorithms, simulation, and cryptographic protocols. Among QW models, the DTQW is particularly suited for circuit implementation on quantum computers due to its natural discretization of both time and space [7].

A. Discrete-time quantum walk on a cycle

In the DTQW, the walker is quantum-mechanical system which possesses two degrees of freedom: position and an internal two-level coin system. Hence, the dynamics of the walker are described by a complex Euclidean space that is the tensor product of the coin and position spaces. Thus, the entire dynamics takes place in the space

$$\mathcal{H} = \mathcal{H}_C \otimes \mathcal{H}_P = \mathbb{C}^2 \otimes \mathbb{C}^N, \quad (1)$$

where N is the number of positions on the cycle [3, 18].

Each step of the walk is described by the unitary operator

$$U = S(C \otimes \mathbb{1}_{\mathcal{H}_P}), \quad (2)$$

where $C \in U(\mathbb{C}^2)$ is a unitary coin operator, $\mathbb{1}_{\mathcal{H}_P}$ is the identity on the position space, and S is the conditional shift operator. The operator S moves the walker clockwise or counterclockwise around the cycle, conditioned on the coin state:

$$S|s_C\rangle|j_P\rangle = |s_S\rangle|(j + 2s - 1) \bmod N\rangle_P, \quad (3)$$

where $s \in \{0, 1\}$ and $j \in \{0, \dots, N - 1\}$.

B. Quantum circuit design

Efficient implementation of DTQW circuits is crucial for their applicability on current quantum hardware. The design presented in [7] achieves a significant reduction in multi-qubit gate count and circuit depth compared to earlier approaches. For a DTQW on a $N = 2^n$ -cycle over t steps, their scheme requires only $O(n^2 + nt)$ two-qubit gates, as opposed to the $O(n^2t)$ scaling of previous QFT-based schemes.

The key innovation is the diagonalization of the conditional shift operator using the quantum Fourier transform (QFT) without swap gates, $\tilde{\mathcal{F}}$:

1. Apply $\tilde{\mathcal{F}}$ to the position register.
2. In the Fourier basis, each time step consists of a layer of single-qubit and controlled phase gates acting conditionally on the coin state, together with the coin operator.
3. Apply the inverse QFT to the position register.

The resulting operator for t steps is:

$$U^t = (\mathbb{1}_C \otimes \tilde{\mathcal{F}}^\dagger) [\Sigma(C \otimes \mathbb{1}_P)]^t (\mathbb{1}_C \otimes \tilde{\mathcal{F}}), \quad (4)$$

where Σ is a diagonal operator in the Fourier basis, applying different phase shifts to the position states depending on the coin state. It has the form:

$$\Sigma = |0_C\rangle\langle 0_C| \otimes \Omega^\dagger + |1_C\rangle\langle 1_C| \otimes \Omega, \quad (5)$$

and

$$\Omega = \text{diag}(1, e^{2\pi i/N}, e^{4\pi i/N}, \dots, e^{2\pi i(N-1)/N}) = \bigotimes_{k=1}^n R_k. \quad (6)$$

with

$$R_k = \begin{pmatrix} 1 & 0 \\ 0 & e^{2\pi i/2^k} \end{pmatrix}. \quad (7)$$

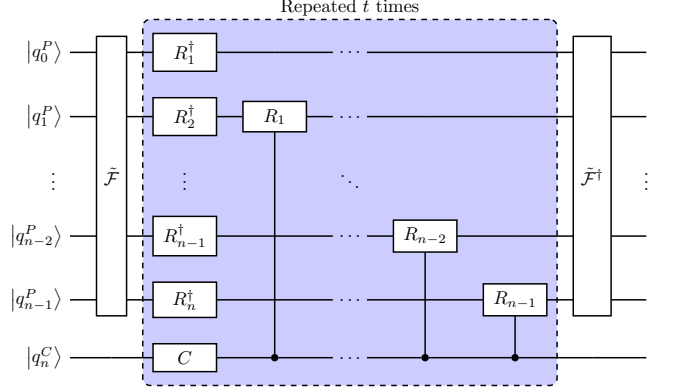


FIG. 1. Quantum circuit for a discrete-time quantum walk on a cycle with n position qubits. The quantum Fourier transform, $\tilde{\mathcal{F}}$ and its inverse do not contain the SWAP operations (see [19] for details). The operations R_k are defined in Eq. (7)

Fig. 1 shows the circuit, illustrating that only one QFT and one inverse QFT are needed, regardless of t , with the central block repeated for each time step. This approach can be further simplified for an initially localized walker (in the state $|\phi_C\rangle|0_P\rangle$) by replacing the QFT with a layer of Hadamard gates (see Appendix B in [7]).

III. QUANTUM IMAGE ENCRYPTION BASED ON QUANTUM WALKS

In this section, we recall a quantum image encryption algorithm introduced in [1]. This algorithm will leverage

the intrinsic unpredictability and complexity of quantum walks, particularly DTQWs, to generate robust cryptographic keys. These keys secure quantum images represented using the Novel Enhanced Quantum Representation (NEQR).

We will encode using the NEQR model, storing grayscale pixel intensities in quantum registers. Each pixel intensity is represented as an 8-qubit quantum state, facilitating direct manipulation through quantum circuits. Formally, an image with dimensions $2^n \times 2^n$ is represented as:

$$\mathbb{C}^8 \otimes \mathbb{C}^n \otimes \mathbb{C}^n \ni |I\rangle = \frac{1}{2^n} \sum_{i=0}^{2^n-1} \sum_{j=0}^{2^n-1} |c_{i,j}\rangle \otimes |ij\rangle, \quad (8)$$

where $|c_{i,j}\rangle$ encodes the grayscale value, and $|ij\rangle$ indicates pixel position.

The cryptographic key is derived from a DTQW performed on an N -node cycle. This quantum walk evolves according to:

$$U = S(C \otimes \mathbb{1}), \quad (9)$$

with C being the coin operator and S is the shift operator. After r iterations, the final state of the quantum walker yields a probability distribution $\{p_i\}_{i=1}^N$. The walk is implemented using the procedure described in Section II B.

The coin operator C can alternate among three distinct configurations C_0 , C_1 , and C_2 , depending on a binary message m . The three coin operators are parameterized as follows:

$$\hat{C}_0 = \begin{pmatrix} \cos \theta_1 & \sin \theta_1 \\ \sin \theta_1 & -\cos \theta_1 \end{pmatrix}, \quad (10)$$

$$\hat{C}_1 = \begin{pmatrix} \cos \theta_2 & \sin \theta_2 \\ \sin \theta_2 & -\cos \theta_2 \end{pmatrix}, \quad (11)$$

$$\hat{C}_2 = \begin{pmatrix} \cos \theta_3 & \sin \theta_3 \\ \sin \theta_3 & -\cos \theta_3 \end{pmatrix}. \quad (12)$$

During the quantum walk, the selection among these coin operators at each step is guided by the binary message m , where each bit of m determines the specific coin operator used at that step. If the quantum walk exceeds the length of m , coin operator C_2 is consistently applied.

A. Encryption Procedure

The encryption algorithm consists of three main steps:

1. Perform a DTQW on a cycle using parameters $(m, N, r, \theta_1, \theta_2, \theta_3)$, such that N is a square of a natural number, producing a probability distribution $\{p_i\}_{i=1}^N$.
2. Convert the obtained probability distribution $\{p_i\}_{i=1}^N$ into an integer-valued grayscale matrix through the transformation:

$$s_{i,j} = \text{floor}((p_{i,j} \times 10^8) \bmod 256), \quad (13)$$

where $p_{i,j}$ are the entries of the probability distribution reshaped into a matrix

3. Encode the matrix $s_{i,j}$ into a quantum state

$$|K\rangle \propto \sum_{i,j} |s_{i,j}\rangle \otimes |ij\rangle, \quad (14)$$

using NEQR encoding, creating a quantum key image.

4. Encode the original image into a quantum state

$$|I\rangle \propto \sum_{i,j} |c_{i,j}\rangle \otimes |ij\rangle, \quad (15)$$

obtaining a combined quantum state of the key and the image:

$$|\psi\rangle \propto \sum_{i,j} |s_{i,j}\rangle \otimes |c_{i,j}\rangle \otimes |ij\rangle. \quad (16)$$

5. Encrypt the original quantum NEQR image $|I\rangle$ by applying quantum controlled-NOT (CNOT) gates. The quantum key image $|K\rangle$ acts as the control, and $|I\rangle$ as the target, yielding the encrypted quantum image and key state:

$$|\phi\rangle = (\text{CNOT} \otimes \mathbb{1}) |\psi\rangle \propto \sum_{i,j} \text{CNOT}(|s_{i,j}\rangle \otimes |c_{i,j}\rangle) \otimes |ij\rangle, \quad (17)$$

B. Decryption Procedure

Decryption involves reversing the encryption steps by applying the same quantum key as control qubits on the encrypted image, using CNOT gates. This procedure successfully retrieves the original image.

IV. RESULTS AND DISCUSSION

Due to the switching of the coin operators, the quantum walk has potential to exhibit the Parrondo paradox. Here we will study both cases and argue that the Parrondo paradox area of parameters should be avoided in the encryption protocol. To show this point we will study a selection of 64x64 pixel images.

A. Case I: no paradox

In Fig. 2 we show the results of the encryption protocol for the case when the quantum walk does not exhibit the Parrondo paradox. The images are encrypted using the quantum walk and later decrypted using the same quantum walk protocol. In this case the parameters of the quantum walk used to encrypt the images are:

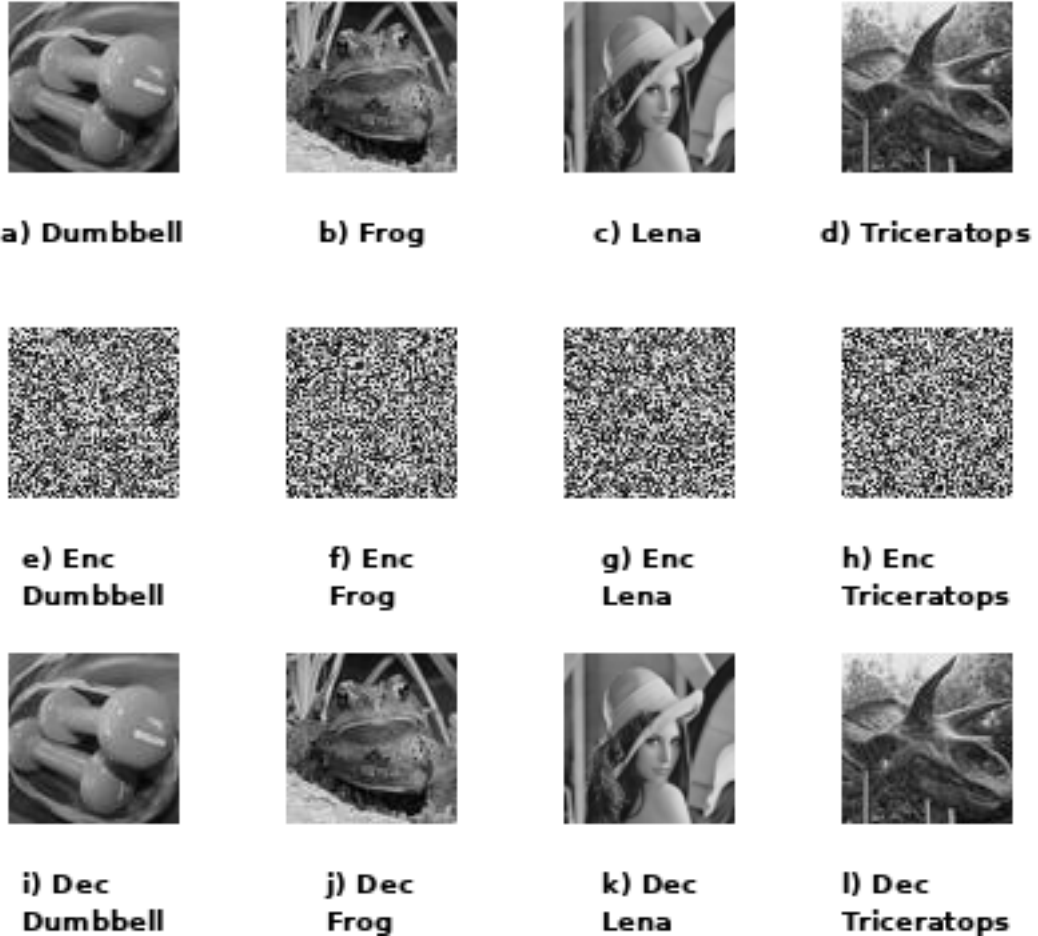


FIG. 2. Example results of the quantum image encryption protocol for the case when the quantum walk does not exhibit the Parrondo paradox. The first row shows the original images, the second row shows the encrypted images, and the third row shows the decrypted images. The images are 64x64 pixels in size.

- $N = 2^8$ (the number of positions on the cycle),
- $r = 128$ (the number of steps of the quantum walk),
- $m = 0011001100\dots$ (the binary message used to select the coin operators),
- $\theta_1 = 0.1$,
- $\theta_2 = 0.2$,
- $\theta_3 = 0.3$.

We start the analysis of the results by computing the correlation coefficients between the pixel values of the original and encrypted images. The correlation coefficients are computed for the horizontal (C_H), vertical (C_V), and diagonal (C_D) directions. These coefficients were calculated using the equation

$$C_{xy} = \frac{\sum_{i=1}^M (x_i - \bar{x})(y_i - \bar{y})}{\sqrt{\sum_{i=1}^M (x_i - \bar{x})^2 \sum_{i=1}^M (y_i - \bar{y})^2}}, \quad (18)$$

where M is the number of adjacent pixels. We average this value for 10^4 random pairs of pixels in the images for each direction. The results are shown in Table I. We see that the correlation coefficients decrease significantly after the encryption, which is a desired property of the encryption protocol. The correlation coefficients for the encrypted images are close to zero, hence no useful information can be extracted from the encrypted images. To further illustrate this point we show the scatter plot of the pixel values of the original and encrypted images in Fig. 3. The scatter plot shows that the pixel values of the encrypted image are uniformly distributed, hence no useful information can be extracted from the encrypted image. This is a desired property of the encryption protocol, as it ensures that the encrypted image does not reveal any information about the original image.

Next, we move to measuring the effect of changing values of pixels in the original image on the encrypted image. This is usually measured by two metrics: the number of pixel change rate (NPCR) and the unified aver-

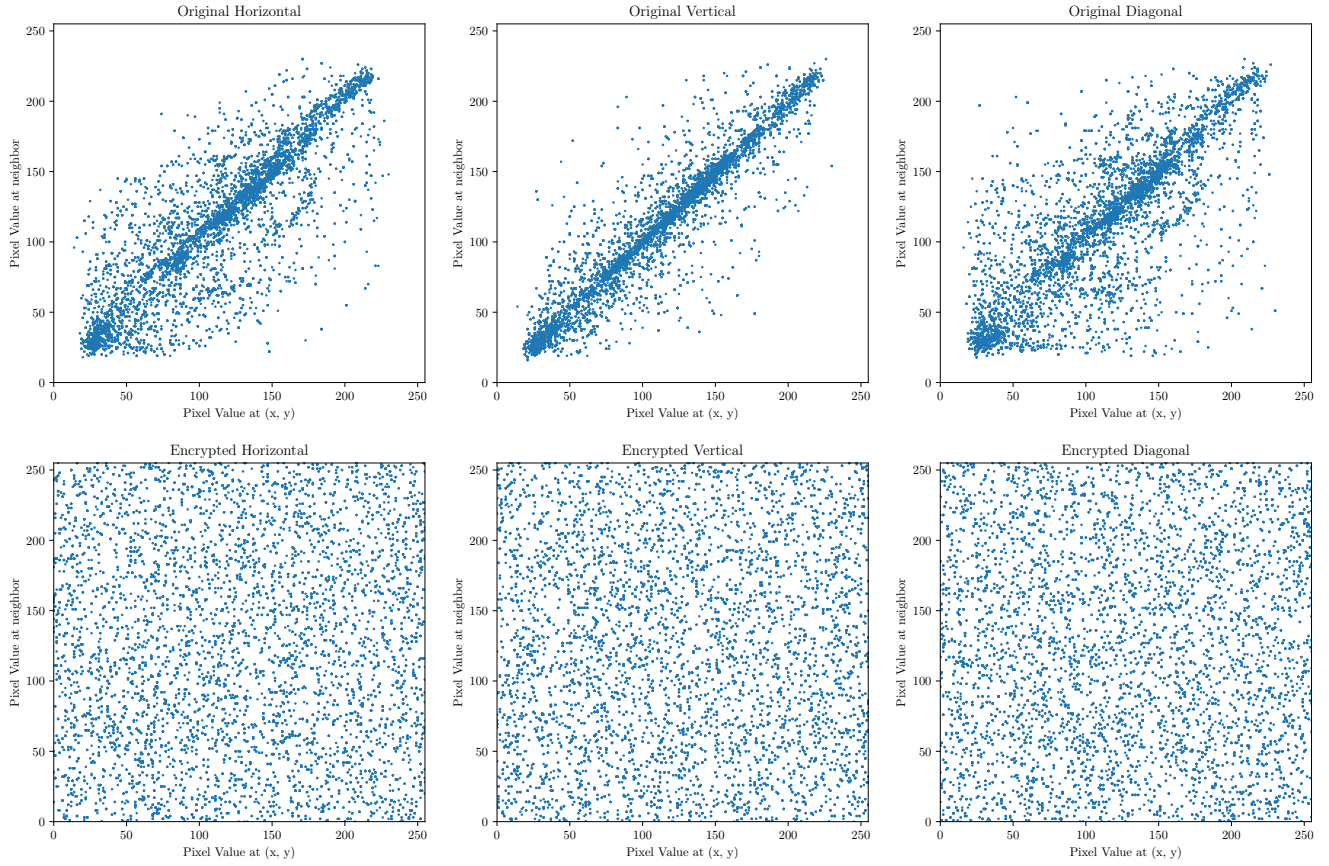


FIG. 3. Scatter plot of the pixel values of the original and encrypted images for the image of Lena. The original image is shown in Fig. 2. The scatter plot shows that the pixel values of the encrypted image are uniformly distributed, hence no useful information can be extracted from the encrypted image.

Filename	C_H	C_V	C_D
dumbbell.png	0.9370	0.8920	0.8452
dumbbell.png (enc)	0.0142	-0.0218	0.0040
frog.png	0.8445	0.8711	0.7852
frog.png (enc)	-0.0246	-0.0154	-0.0365
lena.png	0.8394	0.9361	0.7857
lena.png (enc)	0.0158	0.0115	0.0079
triceratops.png	0.9054	0.8952	0.8391
triceratops.png (enc)	-0.0073	-0.0072	-0.0093

TABLE I. Correlation coefficients for the original and encrypted images. The correlation coefficients are computed for the horizontal (C_H), vertical (C_V), and diagonal (C_D) directions. The values are averaged over the 64x64 pixel images. The original images are shown in Fig. 2.

age changing intensity (UACI). The NPCR is defined as the percentage of pixels that change when a single pixel in the original image is changed. The UACI is defined as the average intensity change of the pixels in the encrypted image when a single pixel in the original image

is changed. The NPCR and UACI are computed using the equations:

$$\text{NPCR} = \frac{1}{M} \sum_{i,j} \mathbb{1}_{\{I_{i,j} \neq I'_{i,j}\}}, \quad (19)$$

where M is the number of pixels in the image, I is the original image, I' is the encrypted image, and $\mathbb{1}$ is the indicator function. The UACI is defined as:

$$\text{UACI} = \frac{1}{M} \sum_{i,j} \frac{|I_{i,j} - I'_{i,j}|}{2^N - 1}, \quad (20)$$

where N is the number of bits used to represent the pixel values. The results are shown in Table II. We see that the NPCR is close to 100% and the UACI is close to 0.33, which is a desired property of the encryption protocol. This means that changing a single pixel in the original image changes almost all pixels in the encrypted image, and the average intensity change is close to the maximum possible value. Again, this shows that the encryption protocol is secure and does not reveal any information about the original image.

Filename	NPCR (%)	UACI (%)
dumbbell.png	99.3896	28.9404
frog.png	99.6582	31.2180
lena.png	99.3652	29.0209
triceratops.png	99.5117	30.5525

TABLE II. NPCR and UACI for the original and encrypted images. The values are averaged over the 64x64 pixel images. The NCPR is close to 100% and the UACI is close to 0.33, which is a desired property of the encryption protocol.

Next, we analyze the histogram of the pixel values of the encrypted images. This is a very simple tool which can clearly visualize the performance of the encryption protocol. A good encryption protocol should produce an encrypted image whose histogram is uniform, i.e. all pixel values are equally likely. In Fig. IV A we show the histograms of the pixel values of the original and encrypted images. The histograms are computed for the 64x64 pixel images. We see that the histograms of the encrypted images are uniform, while the histograms of the original images are not.

Finally, we will analyze the entropy of the pixel values of the encrypted images. The entropy is a measure of the uncertainty of the pixel values, and it is defined as:

$$H(X) = - \sum_{i=0}^{255} p_i \log_2 p_i, \quad (21)$$

where p_i is the probability that a pixel has the value i . The entropy is maximal when all pixel values are equally likely, i.e. $p_i = 1/256$ for all i , hence $H(X) = 8$ in such a case. The results are shown in Table III. We see that the entropy of the pixel values of the encrypted images is close to 8, which is a desired property of the encryption protocol. This means that the pixel values of the encrypted images are uniformly distributed, and hence no useful information can be extracted from the encrypted images.

Filename	H_{orig}	H_{enc}
lena.png	7.5122	7.9541
frog.png	7.6228	7.9596
dumbbell.png	7.3491	7.9583
triceratops.png	7.5429	7.9606

TABLE III. Entropy of the pixel values of the original and encrypted images. The entropy is computed for the 64x64 pixel images. The entropy of the pixel values of the encrypted images is close to 8, which is a desired property of the encryption protocol. This means that the pixel values of the encrypted images are uniformly distributed, and hence no useful information can be extracted from the encrypted images.

B. Case II: Parrondo paradox

Now we will study the case when the quantum walk exhibits the Parrondo paradox. Again, as in the previous case, we will show the results of the encryption protocol for a selection of 64x64 pixel images. The results are shown in Fig. 5. The first row shows the original images, the second row shows the encrypted images, and the third row shows the decrypted images. The images are encrypted using the quantum walk and later decrypted using the same quantum walk protocol.

It can be clearly seen that the images are not encrypted properly. Note that all the encryption parameters are the same as in the previous case, only the coin operators are different. Here we set $\theta_1 = \frac{157}{150}$, $\theta_2 = \frac{157}{900}$, $\theta_3 = \frac{157}{900}$. We identified region of coin parameters where the Parrondo paradox occurs via grid search over the coin parameters θ_1 , θ_2 , and θ_3 . The parameters were sampled in the range $[0, 2\pi]$ with a step size of 0.1.

This shows that the Parrondo paradox can lead to a failure of the encryption protocol. Yet, we will still continue with a full in depth analysis as in the previous subsection. Starting with the correlation coefficients, we compute the correlation coefficients for the horizontal (C_H), vertical (C_V), and diagonal (C_D) directions. The results are shown in Table IV. We see that the correlation coefficients do not decrease significantly after the encryption, which is a sign of failure of the encryption protocol. The correlation coefficients for the encrypted images are close to the original images, hence useful information can be extracted from the encrypted images. To further illustrate this point we show the scatter plot of the pixel values of the original and encrypted images in Fig. 6. The scatter plot shows that the pixel values of the encrypted image are not uniformly distributed, hence useful information can be extracted from the encrypted image. This is a sign of failure of the encryption protocol, as it ensures that the encrypted image reveals information about the original image.

Filename	C_H	C_V	C_D
lena.png	0.8309	0.9349	0.7839
lena.png (enc)	0.1052	0.0814	0.0927
frog.png	0.8475	0.8716	0.7822
frog.png (enc)	0.0673	0.0852	0.0578
dumbbell.png	0.9315	0.8831	0.8511
dumbbell.png (enc)	0.0669	0.0409	0.0854
triceratops.png	0.9058	0.8923	0.8375
triceratops.png (enc)	0.1021	0.1008	0.1070

TABLE IV. Correlation coefficients for the original and encrypted images. The correlation coefficients are computed for the horizontal (C_H), vertical (C_V), and diagonal (C_D) directions.

To continue the analysis, we compute the NPCR and UACI for the original and encrypted images. The results

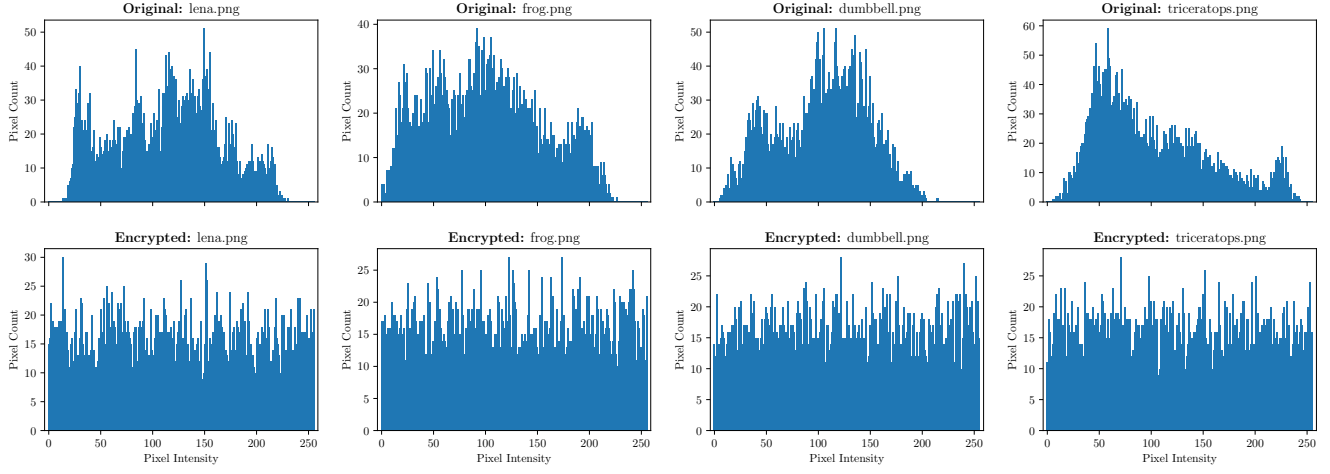


FIG. 4. Histograms of the pixel values of the original and encrypted images. The first row shows the histograms of the original images, and the second row shows the histograms of the encrypted images. The histograms are computed for the 64x64 pixel images. The histograms of the encrypted images are uniform, while the histograms of the original images are not.

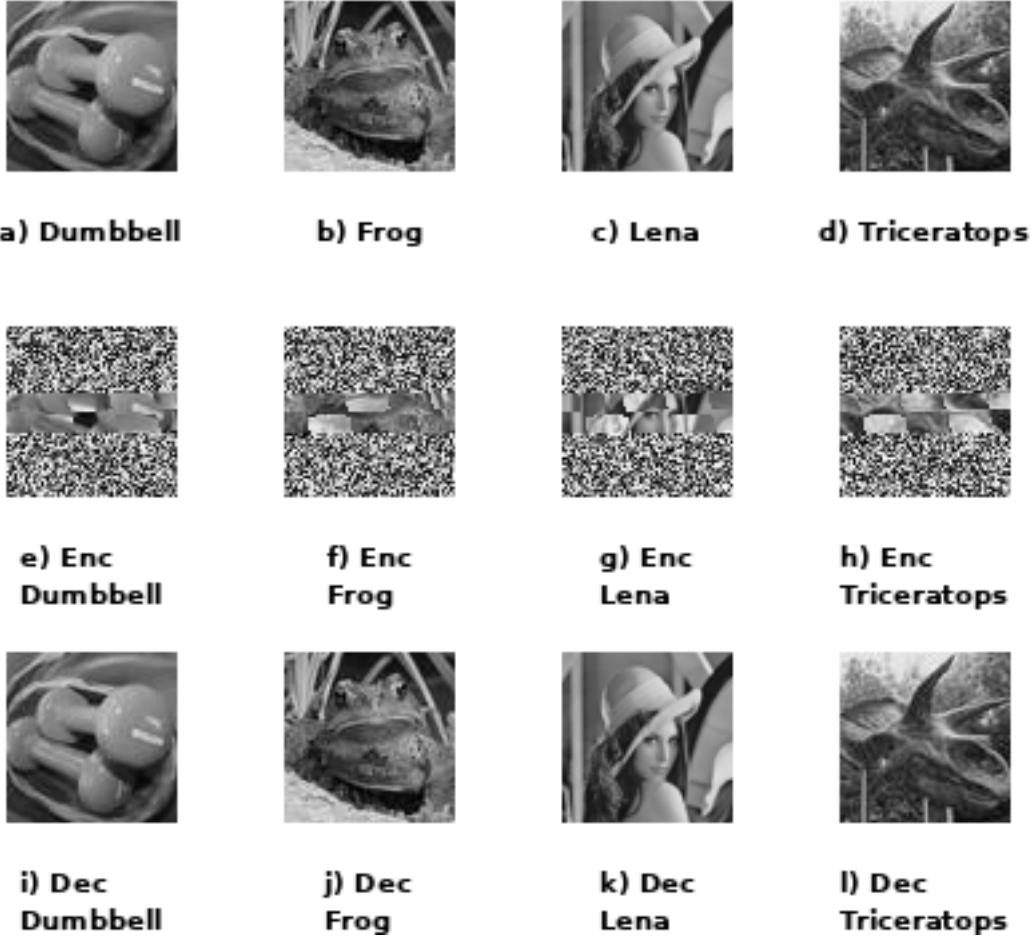


FIG. 5. Example results of the quantum image encryption protocol for the case when the quantum walk exhibits the Parrondo paradox. The first row shows the original images, the second row shows the encrypted images, and the third row shows the decrypted images. The images are 64x64 pixels in size.

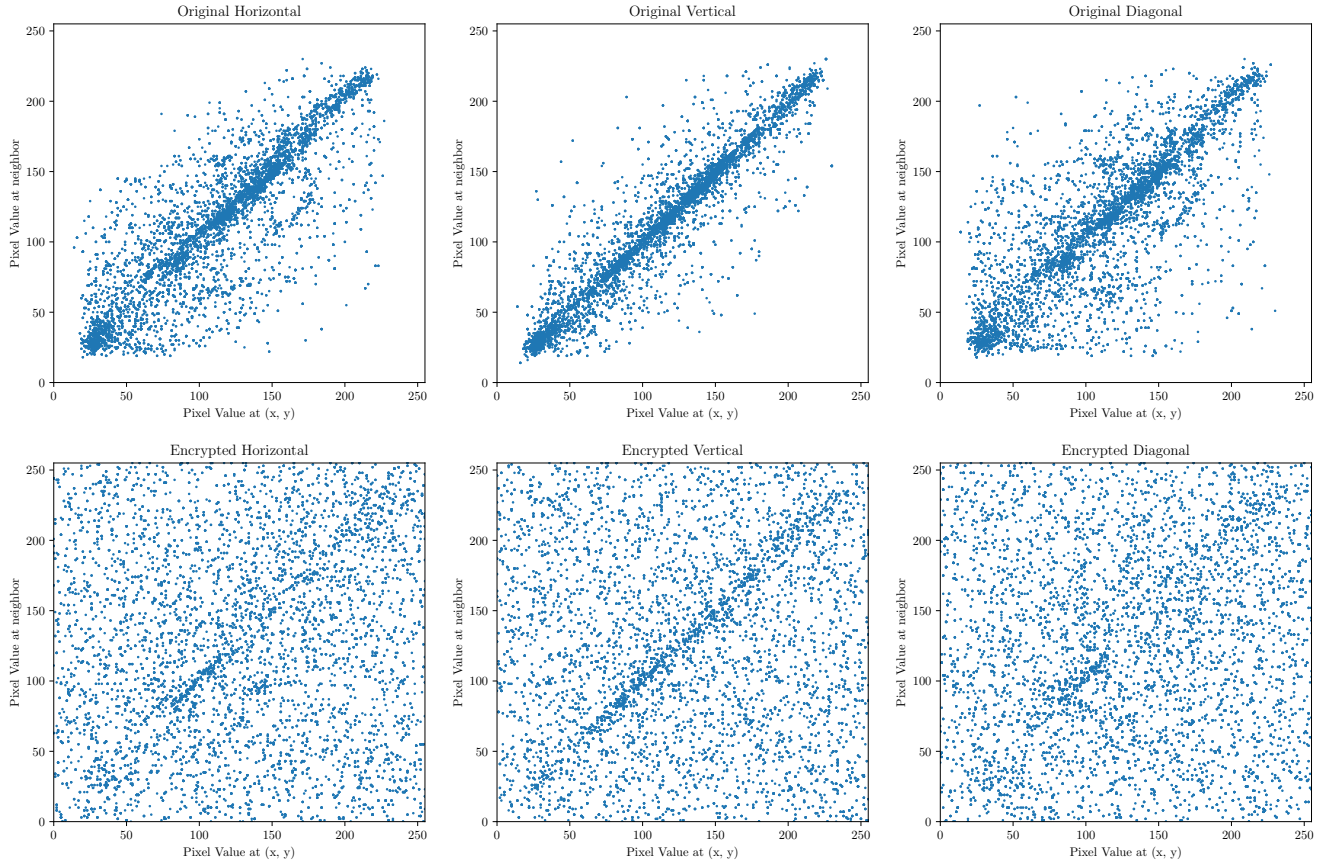


FIG. 6. Scatter plot of the pixel values of the original and encrypted images for the image of Lena. The scatter plot shows that the pixel values of the encrypted image are not uniformly distributed, hence useful information can be extracted from the encrypted image. This is a sign of failure of the encryption protocol, as it ensures that the encrypted image reveals information about the original image.

are shown in Table V. We see that the NPCR is significantly lower than in the previous case, and the UACI is also lower than in the previous case. This is a sign of failure of the encryption protocol. This means that changing a single pixel in the original image does not change almost all pixels in the encrypted image, and the average intensity change is not close to the maximum possible value. Again, this shows that the encryption protocol is not secure and reveals information about the original image.

To finish this analysis we will only show the entropy of the pixel values of the encrypted images. The results are shown in Tab. VI. We see that the entropy of the pixel values of the encrypted images, despite a slight increase, is significantly lower than in the previous case, which is a sign of failure of the encryption protocol. This means that the pixel values of the encrypted images are not uniformly distributed, and hence useful information can be extracted from the encrypted images.

Filename	NPCR (%)	UACI (%)
lena.png	87.6953	26.2432
frog.png	87.7197	26.8716
dumbbell.png	87.7930	24.9889
triceratops.png	87.6953	28.2089

TABLE V. NPCR and UACI for the original and encrypted images. The values are averaged over the 64x64 pixel images. The NPCR is significantly lower than in the previous case, and the UACI is also lower than in the previous case. This is a sign of failure of the encryption protocol. This means that changing a single pixel in the original image does not change almost all pixels in the encrypted image, and the average intensity change is not close to the maximum possible value.

V. CONCLUSIONS

In this manuscript, we have introduced and analyzed a quantum image encryption algorithm based on discrete-time quantum walks (DTQWs), explicitly leveraging the Parrondo paradox phenomenon. By employing quantum

Filename	H_{orig}	H_{enc}
lena.png	7.5122	7.9328
frog.png	7.6228	7.9302
dumbbell.png	7.3491	7.9012
triceratops.png	7.5429	7.9380

TABLE VI. Entropy of the pixel values of the original and encrypted images. The entropy is computed for the 64x64 pixel images. The entropy of the pixel values of the encrypted images is significantly lower than in the previous case, which is a sign of failure of the encryption protocol.

walks on cyclic graphs as generators for cryptographic keys, we have demonstrated a highly sensitive and secure method for quantum image encryption using the Novel Enhanced Quantum Representation (NEQR). Our results underscore that quantum walks provide robust cryptographic keys characterized by complex probability distributions that exhibit inherent unpredictability and sensitivity to initial conditions and operational parameters.

Through detailed simulations, we have shown that the encryption protocol effectively obscures the correlation between adjacent pixels in encrypted images, significantly reducing the correlation coefficients for horizontal, vertical, and diagonal orientations to near-zero values. The analysis of pixel intensity distributions confirms that encrypted images possess uniform histograms, reflecting strong resistance to statistical cryptanalytic attacks. Furthermore, metrics such as the number of pixel change rate (NPCR) and unified average changing intensity (UACI) demonstrate that the algorithm reliably

achieves nearly maximal sensitivity to minor changes in plaintext images, highlighting the encryption scheme's efficacy.

The entropy analysis further supports these findings, with encrypted images consistently approaching the theoretical maximum entropy, indicative of high uncertainty and minimal information leakage. These characteristics collectively affirm the suitability of the proposed encryption method for secure quantum image storage and transmission applications.

Nevertheless, we have also identified conditions under which the Parrondo paradox negatively impacts encryption performance. Specifically, certain combinations of coin parameters causing the paradoxical effect can lead to encryption failure, characterized by reduced entropy, increased correlations, and diminished NPCR and UACI metrics. Thus, careful parameter selection is crucial to avoid the paradoxical region and ensure the consistent reliability of the encryption protocol.

In conclusion, our work highlights the potential and caveats of integrating DTQWs and the Parrondo paradox into quantum cryptographic frameworks, providing clear guidance on parameter selection and implementation considerations. Future research could explore extensions to higher-dimensional quantum walks, real-world hardware implementations, and further enhancements to strengthen cryptographic security.

ACKNOWLEDGMENTS

This work was supported by Institute of Theoretical and Applied Informatics, Polish Academy of Sciences, within the internal project number IITIS/BW/04/25.

[1] B. Abd-El-Atty, A. A. Abd El-Latif, and S. E. Venegas-Andraca, *Quantum Information Processing* **18**, 272 (2019).
[2] Y. Zhang, K. Lu, Y. Gao, and M. Wang, *Quantum information processing* **12**, 2833 (2013).
[3] D. Aharonov, A. Ambainis, J. Kempe, and U. Vazirani, in *Proceedings of the 33rd ACM Symposium on Theory of Computing (STOC 2001)* (ACM, 2001) pp. 50–59.
[4] S. Aaronson and A. Ambainis, *Theory of Computing* **1**, 47 (2005).
[5] N. B. Lovett, S. Cooper, M. Everitt, M. Trevers, and V. Kendon, *Physical Review A—Atomic, Molecular, and Optical Physics* **81**, 042330 (2010).
[6] S. E. Venegas-Andraca, *Quantum Information Processing* **11**, 1015 (2012).
[7] L. Razzoli, G. Cenedese, M. Bondani, and G. Benenti, *Entropy* **26**, 313 (2024).
[8] R. Portugal, *Quantum Walks and Search Algorithms*, 2nd ed. (Springer, Cham, Switzerland, 2018).
[9] K. Kadian, S. Garhwal, and A. Kumar, *Computer Science Review* **41**, 100419 (2021).
[10] D. K. Panda and C. Benjamin, *Physical Review A* **108**, L020401 (2023).
[11] J. M. R. Parrondo, in *ISI* (Torino, Italy, 1996).
[12] J. M. R. Parrondo, G. P. Harmer, and D. Abbott, *Physical Review Letters* **85**, 5226 (2000).
[13] D. Abbott, *Fluctuation and Noise Letters* **9**, 129 (2010).
[14] D. A. Meyer and H. Blumer, *Journal of Statistical Physics* **107**, 225 (2002).
[15] L. Pawela and J. Sładkowski, *Physica D: Nonlinear Phenomena* **256**, 51 (2013).
[16] Z. Walczak and J. H. Bauer, *Physical Review E* **104**, 064209 (2021).
[17] J. W. Lai and K. H. Cheong, *Nonlinear Dynamics* **100**, 849 (2020).
[18] S. E. Venegas-Andraca, *Quantum Information Processing* **11**, 1015 (2012).
[19] Qiskit Development Team, *QFT Class — Qiskit API Documentation*, <https://docs.quantum.ibm.com/api/qiskit/qiskit.circuit.library.QFT> (2025), accessed: 2025-06-18.